Citation: Kechagias-Stamatis, O. & Aouf, N. (2019). H∞ LIDAR odometry for spacecraft relative navigation. IET Radar, Sonar & Navigation, 13(5), pp. 771-775. doi: 10.1049/iet-rsn.2018.5354

This is the accepted version of the paper.

This version of the publication may differ from the final published version. To cite this item please consult the publisher's version.

Permanent repository link: https://openaccess.city.ac.uk/id/eprint/22015/

Link to published version: https://doi.org/10.1049/iet-rsn.2018.5354

IET Radar Sonar and Navigation, Available online 4 January 2019
DOI:10.1049/iet-rsn.2018.5354

H∞ LIDAR Odometry for Spacecraft Relative Navigation

Odysseas Kechagias-Stamatis [1*], Nabil Aouf [1]

[1] Signals and Autonomy Group, Centre for Electronic Warfare Information and Cyber, Cranfield University Defence and Security, Shrivenham, SN6 8LA, UK
[*]o.kechagiasstamatis@Cranfield.ac.uk

Abstract: Current Light Detection and Ranging (LIDAR) based odometry solutions that are used for spacecraft relative navigation suffer from quite a few deficiencies. These include an off-line training requirement and relying on the Iterative Closest point (ICP) that does not guarantee a globally optimum solution. To encounter this, we suggest a robust architecture that overcomes the problems of current proposals by combining the concepts of 3D local feature matching with an adaptive variant of the H∞ recursive filtering process. Trials on real laser scans of an EnviSat model demonstrate that the proposed architecture affords at least one order of magnitude better accuracy compared to ICP.

1. Introduction

Automatic rendezvous and Docking (AR&D) missions for spacecraft applications with non-cooperative targets, i.e. with unknown attitude, is of great interest as currently only cooperative or partially cooperative targets are considered. One major part of the AR&D mission is the precise position estimation of the *Source* spacecraft platform in relation to the *Target* platform. Current solutions for AR&D rely on relative ego-motion estimation, i.e. relative odometry, and involve 2D visual solutions in a stereo camera configuration [1–4] or a monocular [5] camera setup, 2D Infrared (IR) [6] and 3D Light Detection and Ranging (LIDAR) [7–16] relative navigation. The advantage of exploiting the IR domain over the visual is the capability of operating under several harsh illumination conditions such as eclipse and solar glare. Even though [6] presents appealing accuracy, it's performance highly depends on the temperature of the *Target* platform as the latter affects the robustness of IR based local feature detection and matching.

The advantage of 3D LIDAR compared to its 2D counterpart (visual and IR) is operating during day and night, being independent of the target's thermal properties and capable of revealing the underlying structure of an object [17]. Despite current literature offering quite a few LIDAR based relative navigation solutions [7–16], these present the following deficiencies: First, they rely on the Iterative Closest Point (ICP) [18] method that may settle the estimated rigid body transformation solution in a locally rather than a globally optimum solution. Second, current algorithms require an off-line training process that exploits a 3D model of the expected *Target* platform. Even though this is feasible for known manmade objects, unknown or corrupted objects lack of an *a priori* precisely known model. Third, despite [15, 16, 19] transfer computer vision concepts in the domain of space relative navigation, the techniques exploited are regional rather than local, neglecting the state-of-the-art feature matching performance afforded by the latter type. Fourth, the majority of current proposals is evaluated on fully simulated scenarios [9–11, 14–16, 19], while only a few algorithms are tested on real but rather simplistic scenarios [12, 13].

Therefore, driven by the advantages of 3D LIDAR odometry and the deficiencies of the current solutions, we suggest a LIDAR based relative navigation architecture that is appropriate for spacecraft applications. In that context, the contributions and innovations of this work can be summarized to:

a. An odomentry architecture that combines the concepts of 3D local feature matching with an *H∞* recursive filtering process.

b. An adaptive variant of the *H∞* recursive filtering process that adjusts the measurement noise covariance depending on the quality of the matched features.

c. In contrast to current techniques the suggested one does not require any prior knowledge of the *Target* platform.

d. We evaluate our technique on real point clouds acquired by a LIDAR device rather than exploiting synthetic data which is the norm in space odometry literature.

The rest of the paper is organised as follows; Section 2 presents the suggested H∞ LIDAR odometry, while Section 3 evaluates our architecture against the typical ICP method on real laser scans simulating a space relative navigation scenario. Finally, Section 4 concludes this paper.

2. H∞ Lidar Odometry

The problem addressed in this work is LIDAR odometry for spacecraft relative navigation. Specifically, given a *Source* platform that has a 3D LIDAR sensor, we aim at estimating its relative position in regards to a *Target* satellite platform. Therefore, given two consecutive point clouds $\boldsymbol{P}_k = \{p_k^1, ..., p_k^a\}$ and $\boldsymbol{P}_{k+1} = \{p_{k+1}^1, ..., p_{k+1}^b\}$ of the *Target* that are captured from a LIDAR sensor placed on the *Source*, with each vertex being in the form $p_k = (x_k, y_k, z_k)$ and $p_{k+1} = (x_{k+1}, y_{k+1}, z_{k+1})$, aim of the odometry process is to calculate a rigid body transformation

$$R^* = \begin{bmatrix} R & \vert T \\ 0 & \vert 1 \end{bmatrix} \quad (1)$$

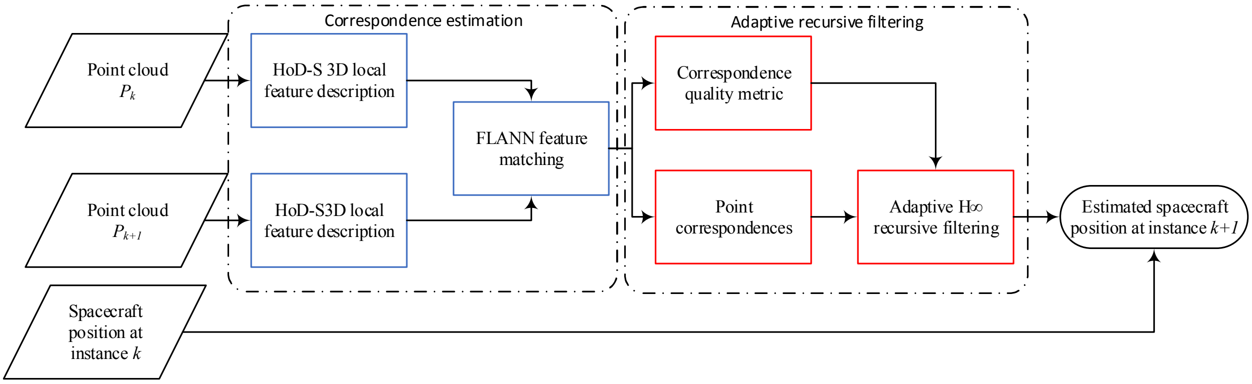

Fig. 1. *Suggested recursive LIDAR based relative navigation.*

with R being the rotation and T the translation component, that maps the source point cloud $\boldsymbol{P}_k$ to the target $\boldsymbol{P}_{k+1}$:

$$p_{k+1} = Rp_k + T \tag{2}$$

$$\begin{bmatrix} x_{k+1} \\ y_{k+1} \\ z_{k+1} \end{bmatrix} = \begin{bmatrix} r_{11} & r_{12} & r_{13} \\ r_{21} & r_{22} & r_{23} \\ r_{31} & r_{32} & r_{33} \end{bmatrix} \begin{bmatrix} x_k \\ y_k \\ z_k \end{bmatrix} + \begin{bmatrix} T_x \\ T_y \\ T_z \end{bmatrix} \tag{3}$$

Then at instance u, the position of the *Source* moving platform relatively to *Target* satellite is given by:

$$R_u^* = \prod_{\mu=1}^{u} R_\mu^* \tag{4}$$

A typical method to estimate R^* is by employing an ICP scheme that involves $\boldsymbol{P}_k$ and $\boldsymbol{P}_{k+1}$. However, as demonstrated in Section 3, the number of available vertices in the satellite's point cloud are very few forcing the ICP registration to settle at a local minima, not accurately register $\boldsymbol{P}_k$ and $\boldsymbol{P}_{k+1}$ and thus provide an inaccurate R^*. Driven by this constraint and the deficiencies of the current solutions presented in Section 1, we suggest an architecture appropriate for space odometry that estimates R^* by combining the concepts of 3D local feature matching with an adaptive variant of the *H*∞ recursive filtering process. The suggested architecture is presented in Fig. 1, and comprises of the two modules presented next.

2.1 *Correspondence Estimation Module*

We describe all vertices belonging to each point cloud $\boldsymbol{P}_k$ and $\boldsymbol{P}_{k+1}$ using a variant of the Histogram of Distances (HoD) [20] entitled HoD-Short (HoD-S) [21, 22]. Despite current literature offering quite a few 3D local feature descriptors such as the Fast Point Feature Histogram (FPFH) [23], Rotational Projection Statistics (RoPS) [17] and Signatures of Histograms of Orientations (SHOT) [24], we used the HoD-S due to its processing efficiency and robustness to highly sparse point clouds [21, 22, 25] as examined in this work.

The operating principle of HoD-S is; for each vertex p_k^i belonging to $\boldsymbol{P}_k$ a spherical volume $\boldsymbol{V}$ of radius ρ that is centred at p_k^i is extracted. Then HoD-S calculates the point-pair L$_2$-norm distance distributions of the vertices within $\boldsymbol{V}$, which are encoded in a coarse manner, i.e. based on a low-resolution distance bin. The description radius used is 20*Res*, where *Res* is the average $\boldsymbol{P}_{k+1}$ resolution and the encoding quality of HoD-S is set to 10 bins. It should be noted that due to the very high sparsity of $\boldsymbol{P}_k$, we intentionally do not use a keypoint detection strategy and therefore describe all vertices belonging to $\boldsymbol{P}_k$.

Let $\boldsymbol{F}_k = \{f_k^1, \ldots, f_k^{N_i}\}$ and $\boldsymbol{F}_{k+1} = \{f_{k+1}^1, \ldots, f_{k+1}^{N_j}\}$ be two sets of HoD-S features for point clouds $\boldsymbol{P}_k$ and $\boldsymbol{P}_{k+1}$ respectively. We match feature f_k^i from $\boldsymbol{F}_k$ with its nearest feature f_{k+1}^j from $\boldsymbol{F}_{k+1}$ based on an L$_2$-norm metric:

$$f_k^i \square f_{k+1}^j \longleftarrow \arg \min_{j=1,2,\ldots,N_j} \left(\left\| f_k^i - f_{k+1}^j \right\|_2 \right) < \tau \tag{5}$$

where *ι,j* are the feature indexes and the threshold τ is experimentally set to 0.8 to remove the majority of the outliers. The matched feature pairs $\{f_k^i, f_{k+1}^j\}$ are considered as feature correspondences, while their associated vertices $\Omega = \left\{ p_k^i, p_{k+1}^j \right\}$ are considered as point correspondences. We speedup the feature matching process of Eq. (5) by employing a Fast Library for Approximate Nearest Neighbours (FLANN) [26] matching scheme. It is worth noting that further reducing τ would provide better quality feature matches but simultaneously reduce the number of matches and in consequence reduce the iterations of the *H*∞ filter as explained in Section 2.2 and ultimately reduce the overall odometry accuracy. In addition, we avoid adding a feature refinement stage as this would increase the processing burden. Current literature suggests global pose-graph optimization, i.e. finding feature matches between non-adjacent frames or applying loop closure. Despite that, in our trials we want to push the limits of a more processing efficient strategy that involves only a Nearest Neighbour feature matching scheme between sequential point clouds.

2.2 *Adaptive Recursive Filtering Module*

Given the correspondences Ω we extend [27] and solve Eq. (3) by suggesting an adaptive *H*∞ recursive filtering scheme. The proposed algorithm is based on a recursive optimal state estimation of the state variable $x_k = [r_{11}\ r_{12}\ r_{13}\ r_{21}\ r_{22}\ r_{23}\ r_{31}\ r_{32}\ r_{33}\ t_x\ t_y\ t_z]^T$ that essentially encompasses the rigid transformation between $\boldsymbol{P}_k$ and $\boldsymbol{P}_{k+1}$ by exploiting the correspondences Ω.

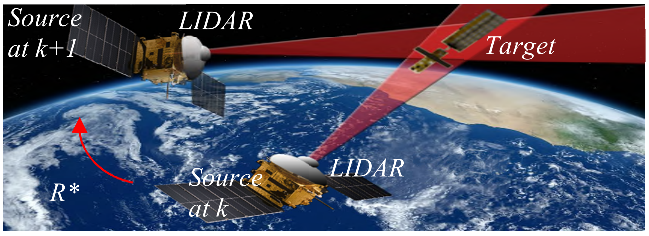

Fig. 2 *Scenario view presenting the Source platform at instance k and k+1 acquiring 3D point cloud data from the Target platform via the onboard LIDAR sensor. R* is the estimated relative motion of the Source to the Target platform based on the suggested HoD-S and adaptive H∞ scheme.*

The *H*∞ filter is a recursive optimal state estimator where x_k is the state variable vector and $\psi_k = [x_k, y_k, z_k]^{\mathrm{T}}$ is the measurement vector that contains the 3D coordinates of the point correspondences p^j_{k+1} belonging to ***P****k+1* which are included in Ω. In this work, we use a slightly modified version of the *H*∞ filter:

$$x_k = \Phi_{k-1} + w_{k-1} \tag{6}$$

$$\psi_k = H_k x_k + v_k \tag{7}$$

where Φ and H are the state transition and the measurement model matrices respectively. We define $\Phi = R^*_0 = [I \mid T_0]$ with *I* the identity matrix and $T_0 = [0\ 0\ 0]^T$, w and v are the model and the measurement noise factors respectively with covariance matrices $W \sim N(0, \sigma^2_w J_{12})$ and $V \sim N(0, M\sigma^2_v J_3)$ where σ_w and σ_v are small positive values and J is the unity matrix. H_k contains the actual measured 3D coordinates of p^i_k belonging to ***P****k* that are included in Ω:

$$H_k = M\begin{bmatrix} x_{k+1} & y_{k+1} & z_{k+1} & 0 & 0 & 0 & 0 & 0 & 0 & 1 & 0 & 0 \\ 0 & 0 & 0 & x_{k+1} & y_{k+1} & z_{k+1} & 0 & 0 & 0 & 0 & 1 & 0 \\ 0 & 0 & 0 & 0 & 0 & 0 & x_{k+1} & y_{k+1} & z_{k+1} & 0 & 0 & 1 \end{bmatrix} \tag{8}$$

with M an adaptive coefficient that aims at adjusting the measurement noise covariance based on the quality of the matched features $\{f^i_k, f^j_{k+1}\}$ defined as:

$$M = 10 \cdot \sum\left(\left|f^i_k - f^j_{k+1}\right|\right) \tag{9}$$

In contrast to the typical *H*∞ filter [28], in this work we suggest an adaptive measurement model matrix *H**k*. The constant in Eq. (9) is experimentally estimated to fine tune the overall *H*∞ filter performance.

The problem that the *H*∞ filter is trying to solve is the $\min_{\hat{x}} \max_{w,v} G$ where G is defined as:

$$G = \frac{average\left(\left\|x_k - \hat{x}_k\right\|\right)_Q}{average\left(\left\|w_k\right\|\right)_W + average\left(\left\|v_k\right\|\right)_V} \tag{10}$$

subject to $G < 1/\gamma$, with Q being a weighting matrix and γ a small constant number representing the required accuracy of the filter. The *H*∞ filter equations solving Eq. (10) are:

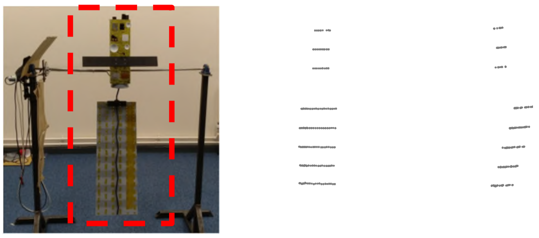
(a) (b) (c)

Fig. 3 *Scaled EnviSat satellite model (a) visual imagery (b)-(c) acquired point cloud in various poses (satellite model enclosed in the dashed red box)*

$$L_k = \left(I - gQP_{k-1} + H^T_k V^{-1} H_k P_{k-1}\right)^{-1} \tag{11}$$

$$K_k = \Phi P_{k-1} L_k H^T_k V^{-1} \tag{12}$$

$$P_k = \Phi P_{k-1} L_k \Phi^T + W \tag{13}$$

$$\hat{x}_{k+1} = \Phi \hat{x}_k + K_k\left(\psi_k - H\hat{x}_k\right) \tag{14}$$

where $Q = Idt$ with $dt = 10^{-5}$ and $g = 0.1$ being regulating parameters. The number of iterations of the H∞ filter is the cardinality of Ω and ultimately the final $\hat{x}$ after all iterations is transformed into R^*, which is input to Eq. (4) in order to estimate the LIDAR odometry. It should be noted that in contrast to our solution, [19] uses a Multiplicative Extended Kalman Filter (MEKF) to smooth R^* rather that estimating the R^* as done in this work. Additionally, [19] requires an offline training stage that uses a known 3D model of the expected *Target* platform, which for our solution is not required.

Space objects typically have symmetric or nearly-symmetric shapes, thus being prone to produce ambiguous measurements. However, in the suggested odometry architecture we reduce the number of such *Target* pose conditions by tuning the description radius of HoD-S to balance features descriptiveness, even in these ambiguous conditions, with processing efficiency. Despite that strategy, a limited number of *Target* poses may still exceed the robustness of HoD-S but our architecture still manages to preserve its robustness via the adaptive recursive filtering module. Specifically, in the event measurements are ambiguous, these are considered as noisy ψ_k values and are compensated within the adaptive *H*∞ filtering process.

3. Experiments

3.1 Experimental Setup

Real laser scans of satellites are not available and therefore we create a number of AR&D scenarios in our Unmanned Autonomous Systems Lab (UASL), simulating a scenario view as presented in Fig. 2. Trials evaluate the suggested LIDAR odometry of a moving platform, i.e. *Source*, in relation to a scaled EnviSat satellite model, i.e. *Target*. Fig. 3 shows the EnviSat model and the acquired ***P****k* in various poses. It should be noted that in order to increase the realistic nature of our scenarios, we discarded the vertices that do not belong to the EnviSat model and thus ultimately each point cloud comprises of approximately 190 vertices. The moving platform utilizes a VLP-16 Velodyne Puck Lite LIDAR to capture the EnviSat point cloud. In

Table 1 Performance metrics for Scenario 1

	e^T_{avg} (m)	$e^T_{\max}$ (m)	drift (m)	T_{error} (%)	t (ms)
ICP	0.408	1.990	0.438	4.38	6
HoD-S+H∞	0.008	0.036	0.140	1.40	59

Table 2 Performance metrics for Scenario 2

	e^T_{avg} (m)	$e^T_{\max}$ (m)	drift (m)	T_{error} (%)	t (ms)
ICP	2.807	7.707	2.697	14.28	13
HoD-S+H∞	0.023	0.081	0.147	0.78	72

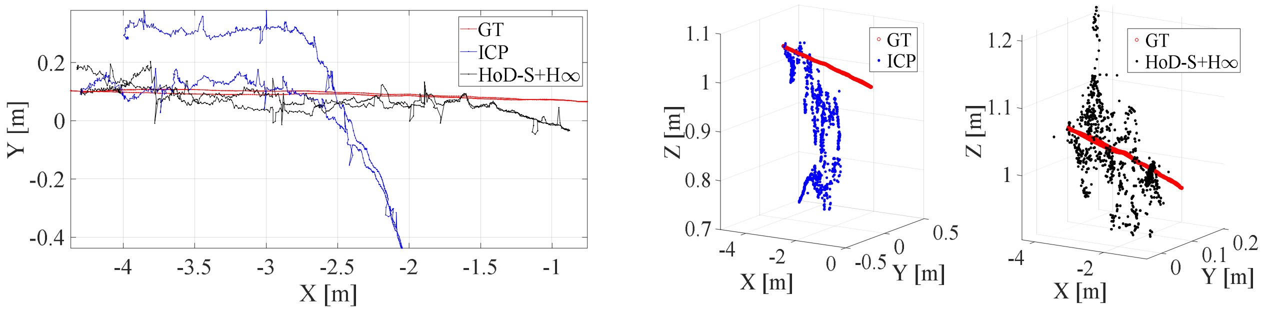

(a) (b)

Fig. 4. *Odometry plots for scenario 1 (a) 2D plot (X-Y projection) (b) 3D plots.*

order to estimate the accuracy of the proposed odometry algorithm, the *Source* is tracked by an Optitrack setup [29] to determine its ground truth position. Optitrack can provide in sub-millimetre accuracy the position of objects that are within its field of view and are visible in the Near Infrared (NIR) bandwidth. For that purpose, we placed on the VLP-16 highly NIR reflective markers.

All trials are implemented in MATLAB on an Intel i7 with 16GB RAM. Even though real space platforms use space-graded Field Programmable Gate Arrays (FPGAs), we believe that in the context of evaluating the conceptual validity and performance of our proposed architecture against current odometry methods, the computer platform used during trials is acceptable.

3.2 Evaluation Criteria

Similarly to current literature [9, 15, 16, 30], we compare the accuracy of the suggested architecture against an optimally tuned ICP registration process. We use a point-to-point ICP, while odometry performance is evaluated based on the average and the maximum tri-axial translational error between the ground truth position of the moving platform (GT) as tracked by the Optitrack and the estimated one:

$$e^T_{avg} = \sqrt{\frac{1}{u}\sum_{i=1}^{u}\left(\left\| avg(T_{GT}) - avg(T_i^{opt})\right\|^2\right)} \qquad (15)$$

$$e^T_{\max} = \sqrt{\max\left(\left\| avg(T_{GT}) - avg(T_i^{opt})\right\|^2\right)} \qquad (16)$$

where u is the number of point clouds, T_i^{opt} is the transformed translation matrix from the LIDAR reference frame to the Optitrack reference frame in order to make applicable its comparison with the ground truth translation. In addition to these metrics, we also calculate the drift, i.e. RMSE, between the estimated end-point and the GTend-point, the corresponding translational error T_{error} as a percentage over the distance travelled and the average processing time t per *Target* scene.

3.3 Odometry trials

3.3.1 Scenario 1: This scenario considers a forward-backward motion of the moving platform with respect to the EnviSat model. Even though the trajectory might be considered simplistic, it is quite challenging due to the sparsity and limited structure of the EnviSat point cloud (Fig. 2(b) and (c)).

From Table 1 it is evident that the suggested architecture is considerably more accurate than ICP. The suggested architecture performs well for the following reasons. First, HoD-S is robust to highly sparse point clouds [21, 22, 25] providing to the adaptive *H*∞ filter only well-established correspondences. Second, the *H*∞ filter has been designed for robustness against extreme nuisances, and third, the adaptive measurement noise covariance H_k affords further performance improvement over the standard *H*∞ recursive filter.

Fig. 4 presents the trajectory plots of ICP and the suggested HoD-S/ adaptive *H*∞ filter in 2D and in 3D. This figure clearly indicates that the proposed scheme is more accurate than ICP, and still has an affordable processing time in the order of milliseconds (Table 1).

3.3.2 Scenario 2: This scenario is more challenging because in addition to the sparse point cloud of scenario 1, the trajectory is highly curved. Despite that, the accuracy afforded by the proposed architecture is only mildly affected, whereas ICP is heavily affected. Table 2 presents the performance metrics for scenario 2, where it is evident that the suggested combination of HoD-S and adaptive *H*∞ outperforms ICP by a large margin. Similarly to Scenario 1, ICP is faster but given the higher accuracy of the suggested architecture and the processing time of a few milliseconds, the combination of HoD and *H*∞ is quite appealing. Fig. 5 presents the trajectory plots in 2D and in 3D.

3.3.3 Scenario 3: This scenario is even more challenging as is involves a 3D translation of the *Target* platform. Similarly to the previous scenarios, HoD-S combined with the adaptive *H*∞ filter exhibits the superiority of the suggested architecture. Regarding computational time, ICP is more processing efficient but the average 70ms processing time per *Target* scene required by our solution is still quite low. The performance metrics of this scenario are presented in Table 3, while Fig. 6 presents the trajectory

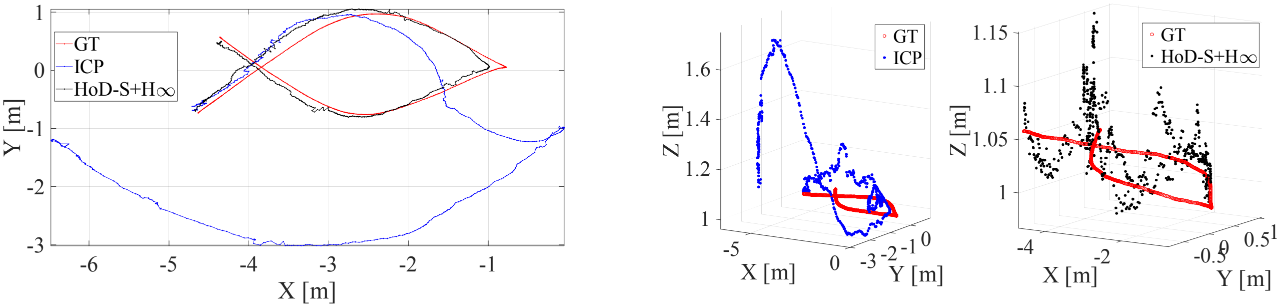

(a)

(b)

Fig. 5. *Odometry plots for scenario 2 (a) 2D plot (X-Y projection) (b) 3D plots.*

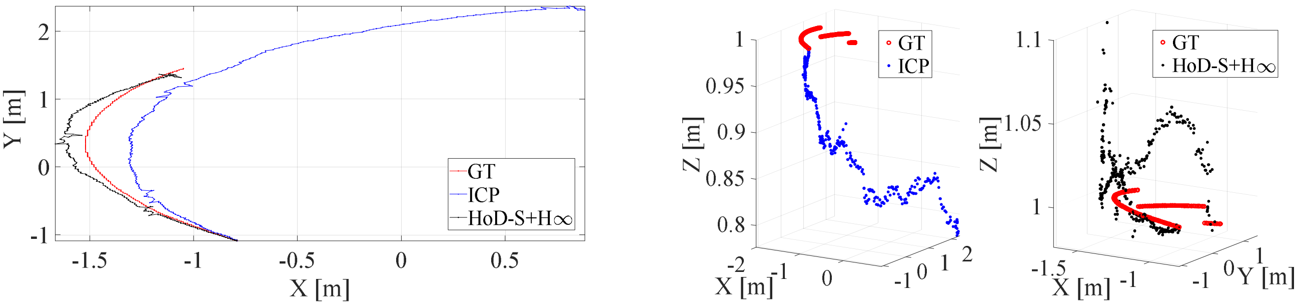

(a)

(b)

Fig. 6. *Odometry plots for scenario 3 (a) 2D plot (X-Y projection) (b) 3D plots.*

Table 3 Performance metrics for Scenario 3

	e^{T}_{avg} (m)	$e^{T}_{\max}$ (m)	drift (m)	T_{error} (%)	t (ms)
ICP	0.975	4.518	2.095	30.59	6
HoD-S+H∞	0.007	0.024	0.125	1.84	70

plots of ICP and the suggested HoD-S/ adaptive $H\infty$ filter.

4. Conclusion

LIDAR based odometry for space relative navigation is a challenging task due to the small number of vertices and the sparsity of the point cloud target. As demonstrated, ICP, which is currently the standard algorithm for space odometry applications, fails to afford accurate space relative navigation. Therefore, we propose a robust architecture appropriate for space odometry that combines a HoD-S based 3D local feature matching with an adaptive $H\infty$ recursive filtering. The advantages of our technique against current solutions are neglecting the requirement of an off-line training process, the need of a priori knowledge of the expected *Target* platform, and exploiting 3D local feature based concepts rather than regional ones. The accuracy of the suggested algorithm is tested on real laser scans of an EnviSat satellite model, where we demonstrate that the proposed architecture is an appealing solution outperforming ICP and affording at least one order of magnitude better accuracy compared to ICP.

As future work, we intend to investigate alternative recursive filtering algorithms and extend to even more complex both real and simulated scenarios. It would be also interesting to implement embedded hardware in the loop recursive filtering registration

5. References

1 Li, L., Lian, J., Guo, L., Wang, R.: ‘Visual odometry for planetary exploration rovers in sandy terrains’*Int. J. Adv. Robot. Syst.*, 2013, **10**, pp. 1–7.

2 Tykkala, T., Comport, A.I.: ‘A dense structure model for image based stereo SLAM’*Robot. Autom. (ICRA), 2011 IEEE Int. Conf.*, 2011, pp. 1758–1763.

3 Yang Cheng, Maimone, M., Matthies, L.: ‘Visual Odometry on the Mars Exploration Rovers’*2005 IEEE Int. Conf. Syst. Man Cybern.*, 2006, **1**, pp. 903–910.

4 Maimone, M., Cheng, Y., Matthies, L.: ‘Two years of Visual Odometry on the Mars Exploration Rovers’*J. F. Robot.*, 2007, **24**, (3), pp. 169–186.

5 Krämer, M.S., Hardt, S., Kuhnert, K.: ‘Image Features in Space - Evaluation of Feature Algorithms for Motion Estimation in Space Scenarios’, in ‘Proceedings of the 7th International Conference on Pattern Recognition Applications and Methods’ (SCITEPRESS - Science and Technology Publications, 2018), pp. 300–308

6 Yılmaz O, Aouf N, Majewski L, Sanchez-Gestido M, O.G.: ‘Using infrared based relative navigation for active debris removal’*10th Int. ESA Conf. Guid. Navig. Control Syst.*, 2017, (1), pp. 1–16.

7 Naasz, B.J., Moreau, M.C.: ‘Autonomous RPOD technology challenges for the coming decade’*Adv. Astronaut. Sci.*, 2012, **144**, pp. 403–425.

8 Opromolla, R., Di Fraia, M.Z., Fasano, G., Rufino, G., Grassi, M.: ‘Laboratory test of pose determination algorithms for uncooperative spacecraft’*4th IEEE Int. Work. Metrol. AeroSpace, Metroaerosp. 2017 - Proc.*, 2017, pp. 169–174.

9 Woods, J.O., Christian, J.A.: ‘Lidar-based relative navigation with respect to non-cooperative objects’*Acta Astronaut.*, 2016, **126**, pp. 298–311.

10 Volpe, R., Aerospaziale, I., Università, S., Sabatini, M.: ‘Monocular and Lidar Based Determination of Shape , Relative Attitude and Position of a Non-Cooperative , Unknown Satellite’2017, (September),

pp. 25–29.

11 Gómez Martínez, H., Giorgi, G., Eissfeller, B.: 'Pose estimation and tracking of non-cooperative rocket bodies using Time-of-Flight cameras'*Acta Astronaut.*, 2017, **139**, (February), pp. 165–175.

12 Galante, J., Eepoel, J. Van, Gill, N.: 'Pose Measurement Performance of the Argon Relative Navigation Sensor Suite in Simulated Flight Conditions'*Am. Inst. Aeronaut. Astronaut.*, 2012, pp. 1–26.

13 Sell, J.L., Rhodes, A., Woods, J.O., Christian, J.A., Evans, T.: 'Pose Performance of LIDAR-Based Navigation for Satellite Servicing'*AIAA/AAS Astrodyn. Spec. Conf.*, 2014, (August), pp. 1–14.

14 Song, J.: 'Sliding window filter based unknown object pose estimation'no date.

15 Opromolla, R., Fasano, G., Rufino, G., Grassi, M.: 'Spaceborne LIDAR-based system for pose determination of uncooperative targets'*2014 IEEE Int. Work. Metrol. Aerospace, Metroaerosp. 2014 - Proc.*, 2014, (Dii), pp. 265–270.

16 Opromolla, R., Fasano, G., Rufino, G., Grassi, M.: 'A model-based 3D template matching technique for pose acquisition of an uncooperative space object'*Sensors (Switzerland)*, 2015, **15**, (3), pp. 6360–6382.

17 Guo, Y., Sohel, F., Bennamoun, M., Lu, M., Wan, J.: 'Rotational Projection Statistics for 3D Local Surface Description and Object Recognition'*Int. J. Comput. Vis.*, 2013, **105**, (1), pp. 63–86.

18 Besl, P.J., McKay, N.D.: 'Method for registration of 3-D shapes', in Schenker, P.S. (Ed.): 'Proceedings Volume 1611, Sensor Fusion IV: Control Paradigms and Data Structures' (1992), pp. 586–606

19 Rhodes, A.P., Christian, J.A., Evans, T.: 'A Concise Guide to Feature Histograms with Applications to LIDAR-Based Spacecraft Relative Navigation'*J. Astronaut. Sci.*, 2017, **64**, (4), pp. 414–445.

20 Kechagias-Stamatis, O., Aouf, N.: 'Histogram of distances for local surface description', in '2016 IEEE International Conference on Robotics and Automation (ICRA)' (IEEE, 2016), pp. 2487–2493

21 Kechagias-Stamatis, O., Aouf, N.: 'Evaluating 3D local descriptors for future LIDAR missiles with automatic target recognition capabilities '*Imaging Sci. J.*, 2017, **65**, (7), pp. 428–437.

22 Kechagias-Stamatis, O., Aouf, N., Nam, D.: '3D Automatic Target Recognition for UAV Platforms', in 'Sensor Signal Processing for Defence (SSPD2017)' (2017)

23 Rusu, R.B., Blodow, N., Beetz, M.: 'Fast Point Feature Histograms (FPFH) for 3D registration', in '2009 IEEE International Conference on Robotics and Automation' (IEEE, 2009), pp. 3212–3217

24 Salti, S., Tombari, F., Di Stefano, L.: 'SHOT: Unique signatures of histograms for surface and texture description' *Comput. Vis. Image Underst.*, 2014, **125**, pp. 251–264.

25 Kechagias-Stamatis, O., Aouf, N.: 'A New Passive 3-D Automatic Target Recognition Architecture for Aerial Platforms' *IEEE Trans. Geosci. Remote Sens.*, 2018, pp. 1–10.

26 Muja, M., Lowe, D.G.: 'Fast Approximate Nearest Neighbors with Automatic Algorithm Configuration'*Int. Conf. Comput. Vis. Theory Appl. (VISAPP '09)*, 2009, pp. 1–10.

27 Amamra, A., Aouf, N., Stuart, D., Richardson, M.: 'A recursive robust filtering approach for 3D registration'*Signal, Image Video Process.*, 2016, **10**, (5), pp. 835–842.

28 Simon, D.: 'From here to infinity'*Embed. Syst. Program.*, 2000, (July 2000), pp. 2–9.

29 'Opritrack', https://optitrack.com/, accessed May 2018

30 Opromolla, R., Fasano, G., Rufino, G., Grassi, M.: 'Uncooperative pose estimation with a LIDAR-based system' *Acta Astronaut.*, 2015, **110**, pp. 287–297.